Experimental and Numerical Investigation of Helmholtz resonators and Perforated Liners as Attenuation Devices in Industrial Gas Turbine Combustors

B. Houston, J. Wang, Q. Qin, P. Rubini.*

Acoustics Research Centre, School of Engineering

University of Hull, Kingston upon Hull, England, HU6 7RX

*Corresponding author, p.a.rubini@hull.ac.uk, Tel. +44 (0)1482 465818

Abstract

This paper reports upon developments in the simulation of the passive control of combustion dynamics in industrial gas turbines using acoustic attenuation devices such as Helmholtz resonators and perforated liners.

Combustion instability in gas turbine combustors may, if uncontrolled, lead to large-amplitude pressure fluctuations, with consequent serious mechanical problems in the gas turbine combustor system. Perforated combustor walls and Helmholtz resonators are two commonly used passive instability control devices. However, experimental design of the noise attenuation device is time-consuming and calls for expensive trial and error practice. Despite significant advances over recent decades, the ability of Computational Fluid Dynamics to predict the attenuation of pressure fluctuations by these instability control devices is still not well validated. In this paper, the attenuation of pressure fluctuations by a group of multi-perforated panel absorbers and Helmholtz resonators are investigated both by experiment and computational simulation. It is demonstrated that CFD can predict the noise attenuation from Helmholtz resonators with good accuracy. A porous material model is modified to represent a multi-perforated panel and this perforated wall representation

1

approach is demonstrated to be able to accurately predict the pressure fluctuation attenuation effect of perforated panels. This work

demonstrates the applicability of CFD in gas turbine combustion instability control device design.

Keywords

Combustion Instability

Gas Turbine Combustor

Helmholtz resonator

Perforated liner

CFD

1. Introduction

Recent developments in gas turbine combustion systems, such as Dry Low Emission (DLE)[1] and Dry Low NOx (DLN)[2], have

resulted in a significant reduction in emissions of NOx compared with traditional diffusion type combustors. These reductions have

largely been achieved by the combustion of the majority of fuel in a cool and fuel-lean pre-mixed combustion regime. Burning so close

to the lean limit can however, significantly reduce the stability of the flame and as such significant pressure fluctuations can be formed

within the combustor. Such pressure fluctuations can be magnified when fuel heat release is in phase with inherent combustor acoustic

frequencies and the resultant oscillations can reduce operating efficiently and increase fatiguing of mechanical components, hence

reducing service life and undermining reductions in operational emissions.

Acoustic resonant devices such as Helmholtz Resonators and perforated liners can be tuned such that they attenuate these dynamics,

recouping the efficiency gains and reductions in emissions offered by contemporary combustor technologies. The frequencies at which

the magnitude of combustion instability generated pressure waves are most significant are dependent on many factors such as load conditions, fuel properties and the geometry of the combustor itself. As such the successful attenuation of these instabilities through the use of acoustic resonators relies highly on the ability to tune the resonant device to the same frequency as the detrimental dynamic frequency.

Helmholtz resonators are well proven to be effective at attenuating pressure fluctuations however, they are most effective at a single peak frequency and their attenuation effect decreases rapidly at frequencies away from this peak frequency. In a perforated combustor wall the small perforations and the periphery cooing air form a distributed Helmholtz resonator which can in turn distribute the attenuation of pressure fluctuations across a greater range of frequencies.

Both passive pressure fluctuation attenuation methods still require correct tuning to the detrimental dynamics frequencies, existing analytical formulations cannot accurately consider all the relevant factors in a gas turbine application and experimental design is time-consuming and expensive, often calling for many iterations before arriving at the configuration which is most effective. The application of CFD has been demonstrated to be effective at predicting the pressure fluctuations and acoustic modes inside the combustor[3–6], however its ability to predict the attenuation effects of Helmholtz resonators and perforated walls is still open for validation.

Numerical simulation of a gas turbine combustion system is computationally expensive and as such in this paper the simulation of these two resonant mechanisms are investigated independently of the combustor, so that the intrinsic properties can be analyzed more efficiently and validated against measurements at isothermal atmospheric conditions, before application to a full scale combustor model.

Helmholtz resonators are relatively simple devices, essentially consisting of a neck connected to a resonant cavity, and as such the geometry of the Helmholtz resonator can be readily resolved in a CFD simulation. Simulation of different designs of Helmholtz

resonators can then be compared with measurements and existing analytical models to evaluate the effectiveness of each method in predicting the resultant attenuation of a given design.

In direct contrast, a fully resolved simulation of a multi-hole perforated liner is much more computationally demanding and in this paper, instead of solving for the exact geometry of a perforated liner, a porous media model is introduced and validated. The application of this model allows the attenuation effects of the perforations to be represented without the additional computational cost of fully resolving the intricate geometry of such resonant devices. Using this approach macro-parameters such as the plate thickness, flow resistivity and the porosity are all evaluated and defined in the model. Additionally semi-empirical factors such as end correction length are also included to take the radiation factors of the individual holes into account. As with the Helmholtz resonator the CFD predictions are compared with experimental measurements and existing analytical predictions, both for validation of the CFD methods and evaluation of the analytical methods.

Multi-perforated panel absorber (MPA) is chosen as the benchmark case to validate the ability of porous material models to represent the attenuation effects of perforated plates. MPA is a widely utilized sound absorption device in many existing practical engineering applications such as aerospace, buildings and vehicles. MPAs are easily tuneable and are able to provide high absorption coefficients in both low and medium frequency ranges. Generally speaking, the acoustic absorption properties of perforated plate absorber configuration are determined by the geometric parameters such as plate thickness, perforation size as well as external flow field factors such as the sound pressure level and bias/grazing flow velocity[7,8]. Various analytical and empirical models have been developed by Howe, Maa et al[9–12]to predict the acoustic impedance when mean flow is present or absent. This paper focuses upon the situation where the mean flow is absent. Maa[9] is commonly cited as one of the first authors to deduce an analytical formula describing the acoustic impedance of such resonant devices. Atalla and Sgard[10]also proposed several formulas to predict the impedance of an MPA

4

which has been experimentally validated. These analytical models however are different from the porous material model used in this paper, whose theoretical framework will be presented in next section.

The complete solution of the Navier-Stokes Equations within CFD codes to predict the acoustic properties of a perforated plate absorber has only recently become possible through developments in the capability of CFD codes and computational resources. These recent research examples fully resolved the exact geometry of an isolated periodic element of the perforated wall and solved for each case using large eddy simulation (LES) [13–16]. These authors were however just simulating part of the perforated plate rather than a full scale device by using periodical boundary conditions. Hence it remains that the full spatial and direct numerical CFD solution of a highly perforated region is still very expensive and as such there is a significant benefit to being able to sufficiently represent the attenuation effect of such a region on the surrounding flow field, without the need to spatially resolve the geometry. Very recently, Jourdain and Eriksson[17] presented a non-liner dynamic porous wall model which is able to examine the overall effect of the perforated panels on the flow by applying Bernoulli equation and Newton's second law at the two sides of a perforated panel. They couple this model with an unsteady RANS solver however, the requirement of modification to the core CFD code to encompass analytical models restricts the application in general CFD codes.

The results of this study demonstrate that CFD can be used effectively to fully resolve a discrete Helmholtz resonator and accurately predict the resultant impact on pressure wave fluctuation attenuation, more so to a greater effect than existing analytical methods and that the application of a porous wall model can successfully allow the solution of a perforated wall within a CFD simulation, without the cost of modelling the exact geometry.

5

2. Experimental Methodology

The ability of a Helmholtz resonator to attenuate pressure fluctuations was experimentally determined using a classical impedance tube, as shown in Figure 1. In these experiments a white noise acoustic signal was generated by an audio loudspeaker, the signal propagates along the impedance tube towards the measurement section, where in this case a Helmholtz resonator is located. In this work the characteristic behaviour of the Helmholtz resonator is presented in terms of a frequency dependent pressure ratio, which was measured using a single microphone inside the resonator cavity and a single microphone in the duct wall near the neck of the resonator.

For the MPA the normal incidence sound absorption properties may be classically represented using a transfer function method according to Standard ISO 10534-2[18]. In this procedure the same impedance tube apparatus was used as shown in Figure 1, with the end of the duct capped and the perforated plate mounted inside the duct, leaving a cavity behind the plate. Only the duct wall mounted microphone probe locations were used in this procedure.

3 CFD Methodology

3.1 Governing Equations and Solution Schemes

The behaviour of a continuum fluid flow was obtained in this work by the solution of the three dimensional compressible Navier-Stokes equations using a finite volume method (FVM) solution algorithm. For the compressible viscous flow, the continuity, momentum and energy equations may be presented in a Cartesian coordinate system following [19] as:

$$\frac{\partial \rho}{\partial t} + \mathbf{div}(\rho \vec{\mathbf{u}}) = \mathbf{0} \qquad (1)$$

$$\frac{\partial (\rho u)}{\partial t} + \mathbf{div}(\rho u \vec{\mathbf{u}}) = -\frac{\partial p}{\partial x} + \mathbf{div}(\boldsymbol{\mu} \, \mathbf{grad} \, u) + S_u \qquad (2)$$

$$\frac{\partial (\rho v)}{\partial t} + \mathbf{div}(\rho v \vec{\mathbf{u}}) = -\frac{\partial p}{\partial y} + \mathbf{div}(\boldsymbol{\mu} \, \mathbf{grad} \, v) + S_v \qquad (3)$$

$$\frac{\partial (\rho w)}{\partial t} + \mathbf{div}(\rho w \vec{\mathbf{u}}) = -\frac{\partial p}{\partial z} + \mathbf{div}(\boldsymbol{\mu} \, \mathbf{grad} \, w) + S_w \qquad (4)$$

6

$$\frac{\partial(\rho i)}{\partial t} + \text{div}(\rho i \vec{\mathbf{u}}) = -p \, \text{div} \, \vec{u} + \text{div}(k \, \text{grad} \, T) + \Phi + S_i \qquad (5)$$

and the Equation of State is:

$$p = \rho R T \qquad (6)$$

The above equation set may be represented in the form of a general scalar transport equation:

$$\frac{\partial(\rho \phi)}{\partial t} + \text{div}(\rho \phi \vec{\mathbf{u}}) = \text{div}(\Gamma \, \text{grad} \, \phi) + S_\phi \qquad (7)$$

where ϕ represents $1, u, v, w, i$ (or h), Γ is the appropriate diffusion coefficient for each physical quantity.

To solve the discretized equations, a bounded second order implicit temporal scheme was utilised for the transient term. This implicit scheme is more time-consuming than first order scheme yet has much better solution accuracy, representing the transient term implicitly at current time level, $n + 1$, using the solution from the previous two time steps, n and $n - 1$.

In terms of spatial discretization scheme, a second order upwind scheme was employed to solve for the convective terms. This method has been demonstrated to avoid the dissipative error of typical first order upwind schemes. The diffusion term was modelled by using the central differencing scheme which is of second order accuracy and is able to represent the transportiveness property of diffusion phenomenon.

The pressure gradient term and velocity term coexist and are coupled in the mass and momentum equations. In the present study, a pressure implicit of operator splitting algorithm was employed, which is widely accepted to be appropriate for transient simulations. In the present work, the sound propagation field was represented as viscous laminar flow since the Reynolds number is very small and hence the effects of turbulence may be assumed to be insignificant. A compressible flow solver was employed, even though the mean velocity is very low, because the compressibility of the fluid medium is integral to the transmission of the pressure wave signal and hence should be fully accounted within the CFD solver.

7

3.2 Porous Media model in CFD

For most CFD simulations of porous material, it is not the internal flow details that are of concern. Researchers are, more often than not, interested in the macroscopic effect on the downstream flow. Therefore, rather than resolving every tiny detail in a porous media, key lumped parameters are utilised to reflect the effect of the porous region on the downstream flow. One of the most common parameters is the resistivity coefficient, which can be accommodated in the source term of the momentum transport equations. In the physical-velocity porous media model, the porosity value is accommodated into every term of the three dimensional Navier-Stokes equations to ensure the solution correctly reflects the effect of the true physical velocity within the holes.

The momentum equations for three dimensional flow in porous media are [20]:

$$\frac{\partial(\chi\rho u)}{\partial t} + \text{div}(\chi\rho u\vec{\mathbf{u}}) = -\chi\frac{\partial p}{\partial x} + \text{div}(\mu\,\chi\,\text{grad}\,u) + \chi(S_u + S_{px}) \tag{8}$$

$$\frac{\partial(\chi\rho v)}{\partial t} + \text{div}(\chi\rho v\vec{\mathbf{u}}) = -\chi\frac{\partial p}{\partial y} + \text{div}(\mu\,\chi\,\text{grad}\,v) + \chi(S_v + S_{py}) \tag{9}$$

$$\frac{\partial(\chi\rho w)}{\partial t} + \text{div}(\chi\rho w\vec{\mathbf{u}}) = -\chi\frac{\partial p}{\partial z} + \text{div}(\mu\,\chi\,\text{grad}\,w) + \chi(S_w + S_{pz}) \tag{10}$$

where χ denotes the volumetric porosity.

The porous media body source term S_p can be calculated using the resistivity coefficients and the mean flow velocity at a direction:

$$S_p = -(P_v + P_i \cdot v_p) \cdot v_p \tag{11}$$

where v_p here is the superficial velocity in the source term: $v_p = \chi v$, P_v, P_i denote the resistivity coefficients due to the viscous and inertial effect respectively. The velocity in the impedance tube is very small and the inertial effect is negligible. Thus we can write:

$S_p = -(P_v + P_i \cdot v_p) \cdot v_p \approx -P_v \cdot v_p$. Considering $\Delta P/L = -\sigma * v_p$, viscous resistivity is basically equal to flow resistivity $P_v \approx \sigma$.

The above model was incorporated into the full three dimensional simulation, capable of representing propagation of sound waves in all component directions, both within the fluid medium and the perforated liner.

8

3.3 Acoustic resistivity and End Correction

Flow resistivity is a metric that defines how easily air can pass through a material. The static flow resistivity may be measured according to ISO 9053:1991[21].   For the plate with circular perforations, static flow resistivity may also be estimated by the expression, $\sigma = 32\mu/(\chi d^2)$ according to Stinson and Champoux[22].

However, static resistivity is different from the acoustic resistivity. The dynamic flow resistivity may be estimated by Atalla's method [10] :

$$r = \left(\frac{4t}{d} + 8\frac{\varepsilon_e}{d}\right)\frac{R_s}{\chi}/(t + 2\varepsilon_e) = \sqrt{8\mu\omega\rho_0}/(\chi d) \tag{12}$$

where $R_s = \sqrt{\mu\omega\rho_0/2}$ denotes the surface resistivity due to air flow frication on the surface of the panel. When T=283K. $\rho_0 = 1.2475$kg/m^3 , $\mu = 1.78 \times 10^{-5}$kg/(m s), $\omega = 2\pi f$, viscous resistivity factor can be expressed as:

$$r = 0.03341\sqrt{f}/(\chi d) \tag{13}$$

Based on the above expression, flow resistivity depends only on porosity, hole size, air density and viscosity. In this research, the resistivity was held at a constant value and the frequency was taken to be the estimated resonant frequency of the equivalent single-hole Helmholtz resonator which is the dominant pressure fluctuation frequency through the holes.

Porous media models in typical CFD software are designed for uniform porous media where the flow is even distributed in and around the porous region. However, for a perforated panel with a very low perforation rate, the local minor perforation will lead to flow distortion and sound radiation around the perforation area. This effect can be accommodated by replacing real thickness of the plate t_0 by effective thickness t which includes end correction length.

Ingard and Norris et al[23,24] analyzed the radiation reactance of a circular pipe baffled in an infinite wall. And they approximated the correction length as $0.85d(1 - 1.14\sqrt{\chi})$. The effective perforation thickness was modelled in CFD as:

9

$$t = t_0 + 0.85d(1 - 1.14\sqrt{\chi}) \qquad\qquad (14)$$

where t_0 is the real thickness of the plate and d is the diameter of the perforation and χ the perforation rate. As the end correction

length is added to the plate, the flow resistivity was evenly distributed in the thickness of $(t + 2\varepsilon_e)$.

3.4 Non-reflecting Boundary Conditions

In the majority of CFD simulations, it is necessary to truncate the calculation domain to a bounded size, hence to obtain an accurate

solution of the problem, the conditions at the boundary should be carefully considered. For accurate acoustic simulations, the spurious

wave reflection caused by pressure boundaries is of great significance and can distort the solution of the internal field. A free stream

boundary condition, which is also commonly known as a far-field boundary condition, is one form of non-reflecting boundary condition

and is often applied to external flows. Many alternative variations of non-reflecting boundary conditions exist, each with their own

strengths and weakness [29]. Such boundary conditions are typically based on the assumption of irrotational, quasi-1D flow in the

boundary-normal condition. In this study, the Hybrid Gauss-LSQ gradient method [30] is used to compute the reconstruction gradients

and solve the transport equations at the boundary using the values from the neighbouring cells. The free stream boundary condition

requires the set of pressure, temperature and Mach number to be specified at the boundary. For a typical external flow case these would

be static values however, by specifying synchronized time dependant variations of these values, the boundary can also be used to transmit

an acoustic signal, whilst still retaining its non-reflecting characteristics. This enables the use of the free-stream boundary condition to

effectively represent the inlet of the impedance tube. In this work a Gaussian white noise signal was generated by a MATLAB code,

higher frequencies than the experimental cut-off frequency were filtered out by a low pass filter, ensuring only planar waves are

transmitted and the resultant signal is then amplified to 110dB to emulate the experimental procedure. According to the relations between

10

acoustic pressure, density, temperature and the acoustic velocity, the pressure, temperature and Mach number at inlet free stream

boundary conditions are defined as:

$$\rho' = \frac{p'}{R*T};$$

(15)

$$\rho = \rho' + \rho_0; \ p = p' + p_0;$$

(16)

$$Mach = \frac{p'}{\rho c^2} = \frac{p'}{\gamma*R*T*\rho};$$

(17)

$$T = p/(R*\rho)$$

(18)

where p', ρ' denote the acoustic pressure and acoustic density; p_0, ρ_0 are the atmospheric pressure and density at the experimental

conditions; R is the air gas constant, $R = 287$ J/(Kg · K)); $\gamma = Cp/Cv = 1.4$. Gaussian white noise pressure fluctuations are employed

because it statistically represents all frequencies within the chosen bandwidth..

4. Results & Discussion

4.1 CFD validation

The experimental and CFD methodologies described in the previous sections were employed to model a total of 15 Helmholtz

resonator cases with varying neck diameters of from 3mm to 15mm using the STAR-CCM+ CFD code [28]. A total of three cavity

volumes were used for comparison, consisting of 71,506mm³ (Volume Case 1), 120,850mm³ (Volume Case 2) & 286,020mm³ (Volume

Case 3). The results of the extreme cases of neck diameter and cavity volume are shown in Table 1, where the analytical models are as

described by Ingard[23]. From this it is clear that the CFD simulations agree very well with the measured results, whereas the basic

analytical prediction, is in considerable error across all cases. This is because the analytical model lacks any consideration of the detailed

fluid dynamics at the neck of the resonator, which is why the predictions are always greater than the measured values. By applying the

11

common practice of an end correction equal to 0.85d a reduction in the prediction error can be seen across all cases, however interestingly the more detailed end correction presented by Ingard[23], which considers the impact of diameter ratio of the neck and cavity volume, which should improve the accuracy of the analytical predictions further, demonstrates only a small improvement for the 3mm neck case and a decrease in the accuracy is actually apparent for the 15mm neck case. This is because this model does not consider the impact of the length of the neck (27mm in all cases) or the relationship between the neck length to diameter ratio, and as a result can result in significant error for these cases, when the effect of the length of the neck cannot be neglected.

In Figure 2 it can be seen that the CFD simulations are not sensitive to such factors as they fully resolve the fluid dynamics of the resonator system and therefore can be shown to accurately predict the response for all cases regardless of geometrical factors. Once the CFD has been validated against the measured cases it can then be used to investigate the intrinsic properties of the resonator in more detail. Once such example of how CFD can be used in this way can be seen in Figure 3, where it can be seen that by plotting the time-averaged velocity magnitude against the location in the system (X=0m is the entrance to the neck, Y=0m is the axial centreline) it can be clearly shown that there is a notable difference in the flow regime within the neck and surrounding volume between the two cavity volume cases. Existing analytical methods do not consider such factors, the CFD methods however, can be shown to accurately capture such phenomenon.

The absorption coefficients and acoustic impedance of three perforated plates backed with an air cavity were experimentally measured and numerically predicted using ANSYS Fluent [20]. The porosities range from rather low porosity 0.38% to medium porosity 1.23% and to high porosity 3.41%. Higher porosities were not considered due to their relatively low attenuation capabilities. The experimental data for Plate#1 to Plate #3 was acquired using the experimental facilities described in Section 2. The experimental results for Plate#4 and Plate#5 were obtained from [25,26]

12

Figure 4 presents the absorption coefficients results comparison between CFD, experimental and analytical methods. While all three methods yield similar change trends of absorption coefficient as a function of frequency, there are also some remarkable differences. It is suggested by Figure 4(a) that the empirical method of Atalla and Sgard[10] provides very good agreement with the experimental result. Maa's theory[9] is also accurate in terms of overall trend, but the frequency at a given absorption coefficient is 25-30Hz lower than the frequency with the same absorption coefficient in experiment. CFD predicted absorption coefficient demonstrates a good agreement with experimental results at frequencies lower than the resonant frequency, but the overall absorption band-width tend to be slightly larger than the experimental results. Similar trends can be seen in Figure 4(b), where, compared with experimental data, the absorption band-width predicted by the analytical models is narrower. Both Maa's method and Atalla's method underestimate the absorption coefficient at the resonant frequency by a magnitude of 0.06. The result acquired by CFD simulation is in better agreement with the experimental data compared with those of analytical methods in terms of the absorption band-width. The absorption coefficient at the resonant frequency is 0.05 larger than the experimental result. Different findings are observed in Figure 4(c). Absorption coefficients obtained by the methods of both Maa and Atalla are noticeably lower than those of experiment and CFD. Also the absorption coefficient at the resonant frequency acquired by Atalla's model is only 0.28 while the experiment and CFD give this value of 0.35. This significant error is likely the result of the large perforation diameter (3mm) which will decrease the effectiveness of the analytical models. In comparison, the results from CFD simulation agrees with experimental result much better. Figure 5 compares two different panel absorbers from other references [25,26], it also demonstrates that CFD is able to give generally better agreement with experimental results compared with analytical models.

The relative high absorption frequency range for each MPP is evaluated and listed in Table 3. CFD works as well as Atalla's method in terms of high absorption frequency range for 1mm sized holes perforated panels, but the advantages of CFD over analytical models

13

are obvious for the 3mm perforated panel. Absorption bandwidth predicted by Maa's approach are narrower and more low-frequency inclined. This may be a result of an overestimation of reactance term and underestimation of the resistance term in the Maa's model. Some authors already used larger resistivity term in Maa's equation [26,27]. The high-absorption bandwidth and maximum absorption coefficient acquired by CFD are slightly larger than the experimental one, absorption coefficient and bandwidth obtained by experiment are in turn slight higher than the analytical prediction. This implies that the flow resistivity specified in the CFD simulations is somewhat larger than the real value which is frequency dependent.

In spite of the error which is within reasonable range, CFD has good capability to predict MPAs pressure fluctuation absorption properties with sufficient accuracy.

4.2 Application of CFD on other MPAs

The successful prediction of absorption coefficients on the previous three plates is encouraging. Its application to other cases is undertaken which is listed in Table 4 . Figure 6 and Figure 7 illustrate that CFD and analytical models predict similar trends in which the absorption coefficient changes against frequency. The resonant frequencies acquired by CFD and Atalla and Sgard[10] method agree well. However, as mentioned previously, higher absorption coefficients are predicted by CFD at most frequencies compared with analytical results. Experimental absorption-frequency curves are supposed to lie in between CFD and Atalla's curves. This difference is more clear when the perforation size is large as is shown by Figure 7.

Figure 8 illustrates the variation of absorption coefficients for three panels with the same perforation size (1mm) and different porosities. Both CFD and analytical models predict that the absorption coefficient would decrease and resonant frequency would increase when porosity goes up. The same trend is shown in two cases where the perforation size is 3mm. From another point of view, plate#7 and #10 or plate#2 and #9 or plate #3 and #8 have the same porosity but with different perforation size. Corresponding comparisons

14

demonstrate that the increase of perforation size will lower the resonant frequency and decrease the overall absorption effect of the MPA. This can be explained because larger perforation size leads to a proportionally larger correction length, which would in turn increase the effective length of the plate. On the other hand, larger perforation size brings about lower flow resistivity which brings down the overall absorption effect.

5. Conclusions

The direct geometrical representation of several Helmholtz resonator cases have been simulated, yielding very good agreement with measured data. Geometrically resolved CFD simulations have been shown to produce significantly more accurate peak absorption predictions than existing analytical models and additionally can be used to highlight key differences in the flow regime within the oscillating mass in the neck and radiated regions, which when incorrectly considered in the analytical models is the greatest source of error.

The absorption effect of three perforated panels with low porosity(0.38%), medium porosity(1.23%) and high porosity(3.41%) has been experimentally, numerically and analytically evaluated. The results have demonstrated the capability of CFD in combination with a porous media model in predicting the acoustic properties of MPAs. CFD has been shown to give a good prediction about the absorption band-width and resonant frequency. It has also been demonstrated that CFD can reflect the impact of the panel porosity, perforation size on the resonant frequency and absorption coefficient of a perforated panel absorber. Analytical models provide satisfactory agreement when the hole diameter is small, but their prediction for absorption effect of MPA with large size perforation is less accurate.

In summary, the capability of CFD in predicting the pressure fluctuation absorption effect of Helmholtz resonators and perforated panels has been validated in this paper.

Acknowledgement

Nomenclature

d	equivalent diameter of the perforation	S_ϕ	source term for scalar ϕ
f	frequency	t	effective thickness of the plate
h	enthalpy	t_0	real thickness of the plate
i	internal energy	T	Temperature
p'	acoustic pressure	ρ	density of the medium
p_0	average environment pressure	$\vec{\mathbf{u}}$	the vector of velocity
P_v	viscous resistance	u, v, w	velocity at x, y, z directions of coordinate system.
P_i	inertial resistance	v_p	superficial velocity
r	dynamic flow resistivity	μ	dynamic viscosity
R_s	surface resistivity	ϕ	general scalar($1, u, v, w, i$)
R	gas constant of air	Γ	general diffusion coefficient
S_i	internal energy source term	σ	flow resistance of porous material at low flow velocities
$S_p, S_{px}, S_{py}, S_{pz}$ porous medial body force term		χ	perforation rate
S_u, S_v, S_w velocity source term		ε_e	end correction length at each side of perforation

16

ω angular frequency

ρ_0 average environment air density

ρ' density change due to acoustic pressure

$Mach$ Mac Number

References

[1] Liu K, Sanderson V. The influence of changes in fuel calorific value to combustion performance for Siemens SGT-300 dry low emission combustion system. Fuel 2013;103:239–46.

[2] Evulet AT, ELKady AM, Branda AR, Chinn D. On the Performance and Operability of GE's Dry Low NOx Combustors utilizing Exhaust Gas Recirculation for PostCombustion Carbon Capture. Energy Procedia 2009;1:3809–16.

[3] Orbay RC, Nogenmyr KJ, Klingmann J, Bai XS. Swirling turbulent flows in a combustion chamber with and without heat release. Fuel 2013;104:133–46. doi:10.1016/j.fuel.2012.09.023.

[4] Ranga Dinesh KKJ, Jenkins KW, Kirkpatrick MP, Malalasekera W. Modelling of instabilities in turbulent swirling flames. Fuel 2010;89:10–8.

[5] Gicquel LYM, Staffelbach G, Cuenot B, Poinsot T. Large eddy simulations of turbulent reacting flows in real burners: the status and challenges. J Phys Conf Ser 2008;125:012029.

[6] Roux S, Lartigue G, Poinsot T, Meier U, Bérat C. Studies of mean and unsteady flow in a swirled combustor using experiments, acoustic analysis, and large eddy simulations. Combust Flame 2005;141:40–54.

[7] Sun X, Jing X, Zhang H, Shi Y. Effect of grazing–bias flow interaction on acoustic impedance of perforated plates. J Sound Vib 2002;254:557–73. doi:10.1006/jsvi.2001.4110.

[8] Bellucci V, Flohr P, Paschereit CO. Numerical and Experimental Study of Acoustic Damping Generated by Perforated Screens. AIAA J 2004;42.

[9] Maa D-Y. Potential of microperforated panel absorber. J Acoust Soc Am 1998;104:2861. doi:10.1121/1.423870.

[10] Atalla N, Sgard F. Modeling of perforated plates and screens using rigid frame porous models. J Sound Vib 2007;303:195–208. doi:10.1016/j.jsv.2007.01.012.

[11] Howe M. On the theory of unsteady high Reynolds number flow through a circular aperture. Proc R Soc London 1979;366:205–23.

[12] I. B. Crandall. Theory of Vibrating Systems and Sound by Crandall, I B: D. Van Nostrand Company - Anybook Ltd. 1954:227–30. http://www.abebooks.co.uk/Theory-Vibrating-Systems-Sound-Crandall-B/11322366729/bd.

[13]   Dass J, Mendez S. Large-Eddy Simulation of the Acoustic Response of a Perforated Plate. Am Inst Aeroanutics 2008.

[14]   Mendez S, Eldredge JD. Acoustic modeling of perforated plates with bias flow for Large-Eddy Simulations. J Comput Phys 2009;228:4757–72.

[15]   Mendez BS, Eldredge J, Nicoud F, Poinsot T. Numerical investigation and preliminary modeling of a turbulent flow over a multi-perforated plate. Proc. Summer Progr., 2006.

[16]   Mendez S, Nicoud F, Poinsot T. Large-Eddy Simulation of a Turbulent Flow around a Multi-Perforated Plate. Complex Eff. Large Eddy Simulations, Berlin Heidelberg: 2007, p. 289–303. doi:10.1007/978-3-540-34234-2_21.

[17]   Jourdain G, Eriksson L-E. Numerical Validation of a Time Domain Perforated Plate Model with Nonlinear and Inertial Effects. J Comput Acoust 2014;22:1450009. doi:10.1142/S0218396X1450009X.

[18]   ISO 10534-2:1998 - Acoustics -- Determination of sound absorption coefficient and impedance in impedance tubes -- Part 2: Transfer-function method n.d.

[19]   Malalasekera HKV and W. An Introduction to Computational Fluid Dynamics The Finite Volume Method 2nd Edition | Dler Tahir - Academia.edu. 1995.

[20]   Canonsburg TD. ANSYS FLUENT User ' s Guide 2011;15317:249.

[21]   ISO 9053:1991 - Acoustics -- Materials for acoustical applications -- Determination of airflow resistance n.d.

[22]   Stinson MR. Propagation of sound and the assignment of shape factors in model porous materials having simple pore geometries. J Acoust Soc Am 1992;91:685. doi:10.1121/1.402530.

[23]   Ingard U. On the Theory and Design of Acoustic Resonators. J Acoust Soc Am 1953;25:1037. doi:10.1121/1.1907235.

[24]   Norris AN, Sheng IC. Acoustic radiation from a circular pipe with an infinite flange. J Sound Vib 1989;135:85–93. doi:10.1016/0022-460X(89)90756-6.

[25]   Miasa, I. M, Okuma M, Kishimoto G, Nakahara T. An Experimental Study of a Multi-Size Microperforated Panel Absorber. J Syst Des Dyn 2007;1:331–9. doi:10.1299/jsdd.1.331.

[26]   Jung SS, Kim YT, Lee DH, Kim HC, Cho S Il, Lee JK. Sound Absorption of Micro-Perforated Panel. J Korean Phys Soc 2007;50:1044. doi:10.3938/jkps.50.1044.

[27]   Qin Q, Rubini P, Jayatunga C, Sanderson V. Laboratory investigations of low frequency sound attenuation over combustion flat perforated wall sheet. Acoust. 2012, 2012.

[28] http://www.cd-adapco.com/products/ (accessed September 29th, 2104)

[29] N.K. Singh, Large Eddy Simulation of Acoustic Propagation in Turbulent Flow through Ducts and Mufflers. PhD thesis, Univeristy of Hull, 2012

[30] Shima E, Kitamura K, Fujimoto K. New Gradient Calculation Method for MUSCL Type CFD Schemes in Arbitrary Polyhedra. AIAA 2011-1081
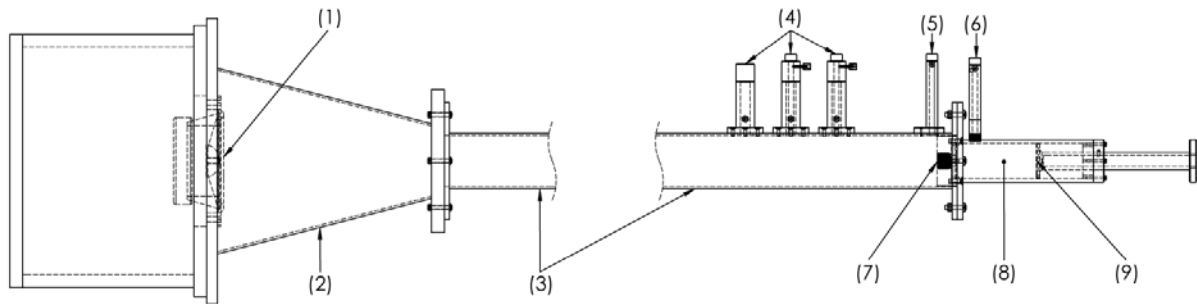
Fig. 1. Impedance tube apparatus used to measure Helmholtz resonator attenuation properties: (1) Box mounted loudspeaker, (2)

Transition duct/Anechoic Section, (3) Square section duct, (4) Duct wall mounted measurement microphone ports, (5) Near-neck, duct

wall mounted measurement microphone port, (6) Resonator wall mounted measurement microphone port, (7) Resonator Neck, (8)

Resonator cavity, (9) Adjustable resonator cavity wall piston

Table.1: Helmholtz resonator configurations and predicted peak absorption frequencies

Neck Diameter (mm)	Volume Case	Peak Absorption Frequency (Hz)				
		Measured	Basic Analytical	0.85D End Correction Analytical	Ingard End Correction[23] Analytical	CFD
3	Case 01	98.42	106.59	101.81	101.30	96.59
3	Case 14	47.61	53.30	50.91	50.20	47.15
15	Case 01	444.64	534.35	438.94	471.63	445.56
15	Case 14	214.54	267.18	219.47	235.77	214.84

21

(a)

(b)

22
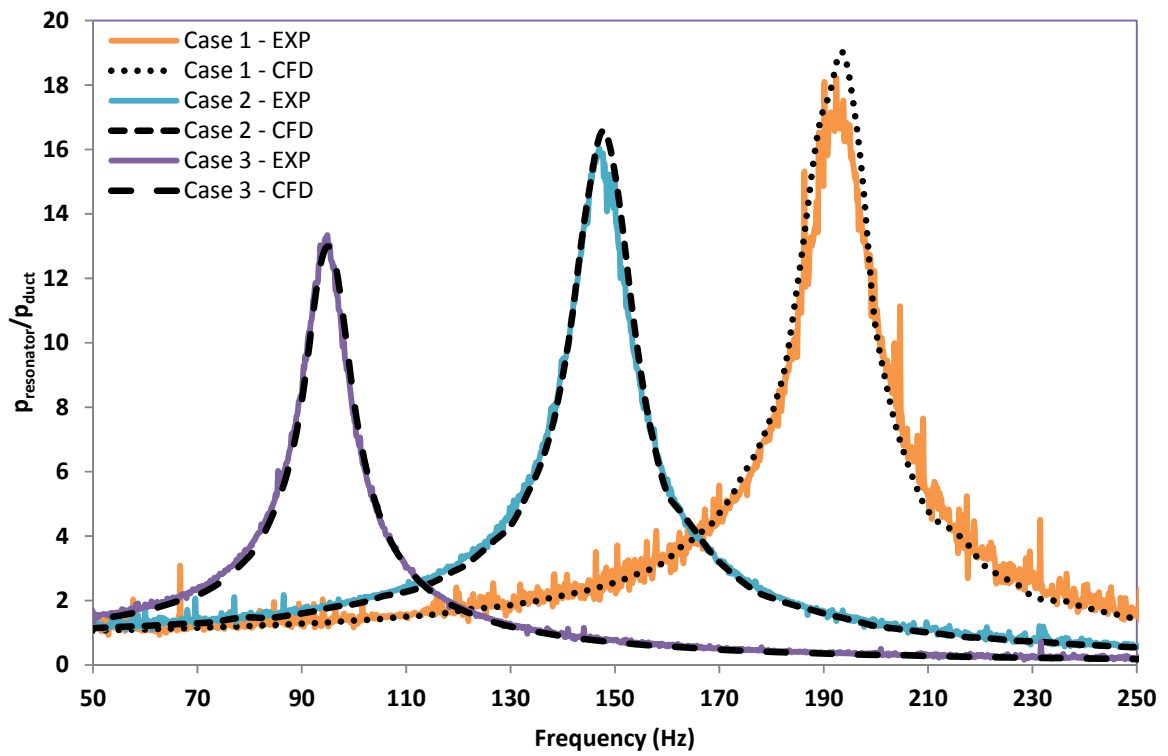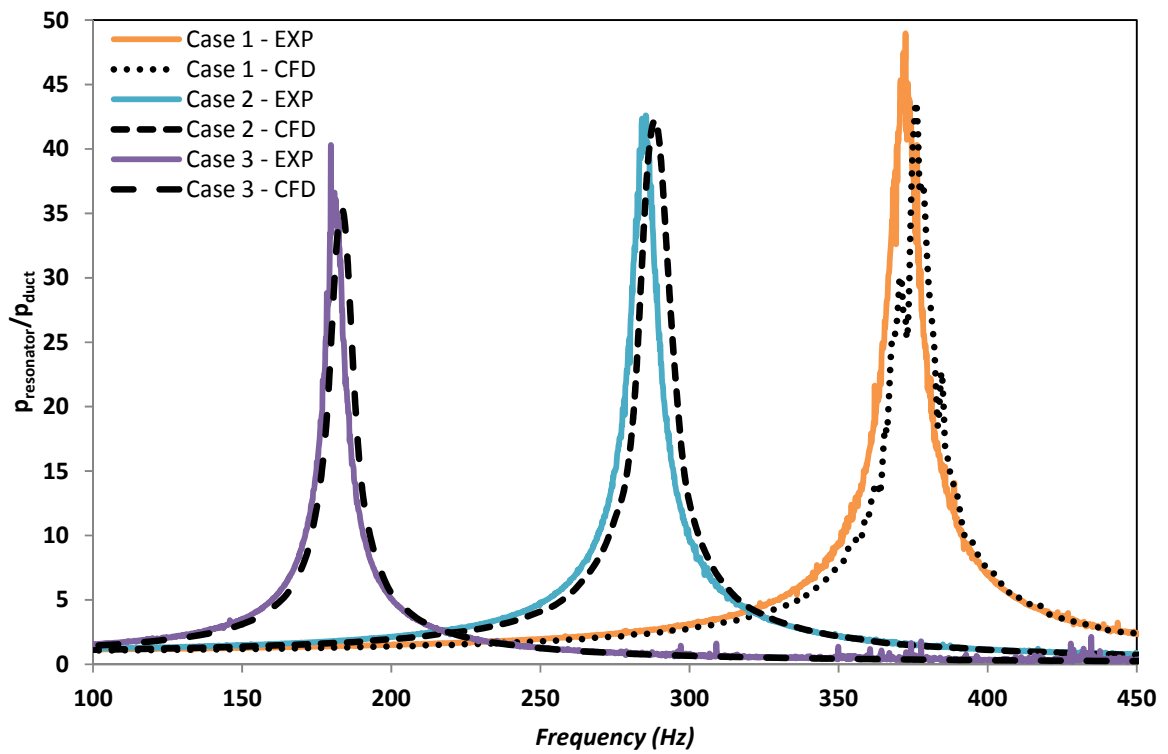
Fig. 2. Experimentally measured and CFD calculated pressure ratio; (a) 6mm Neck Diameter (b) 12mm Neck Diameter
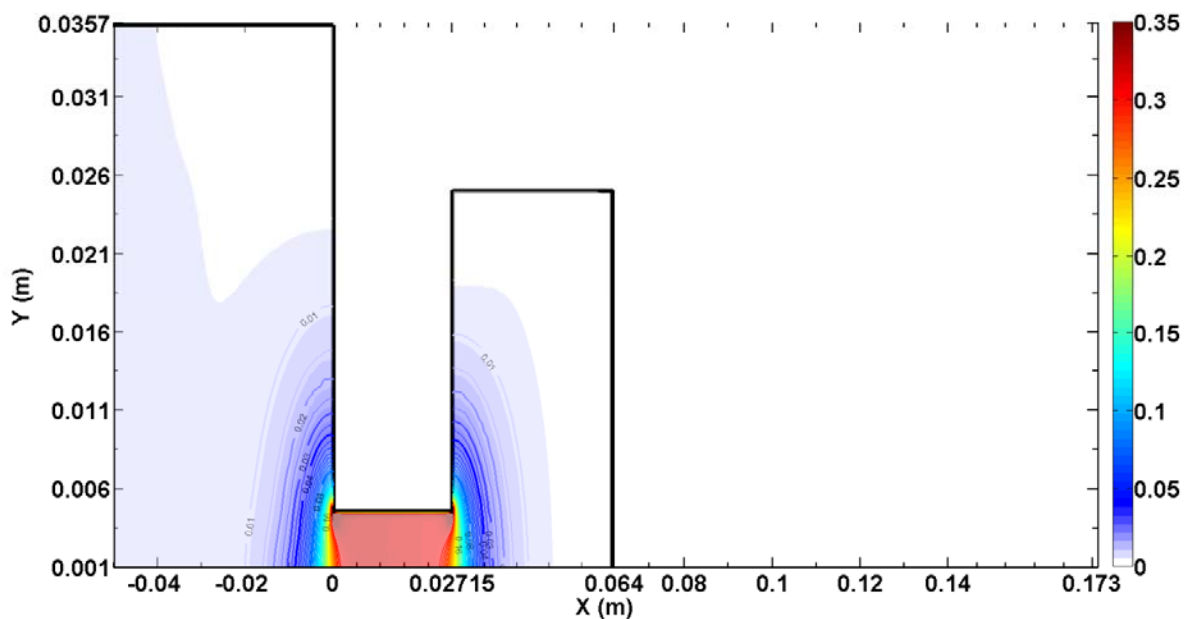
(a)
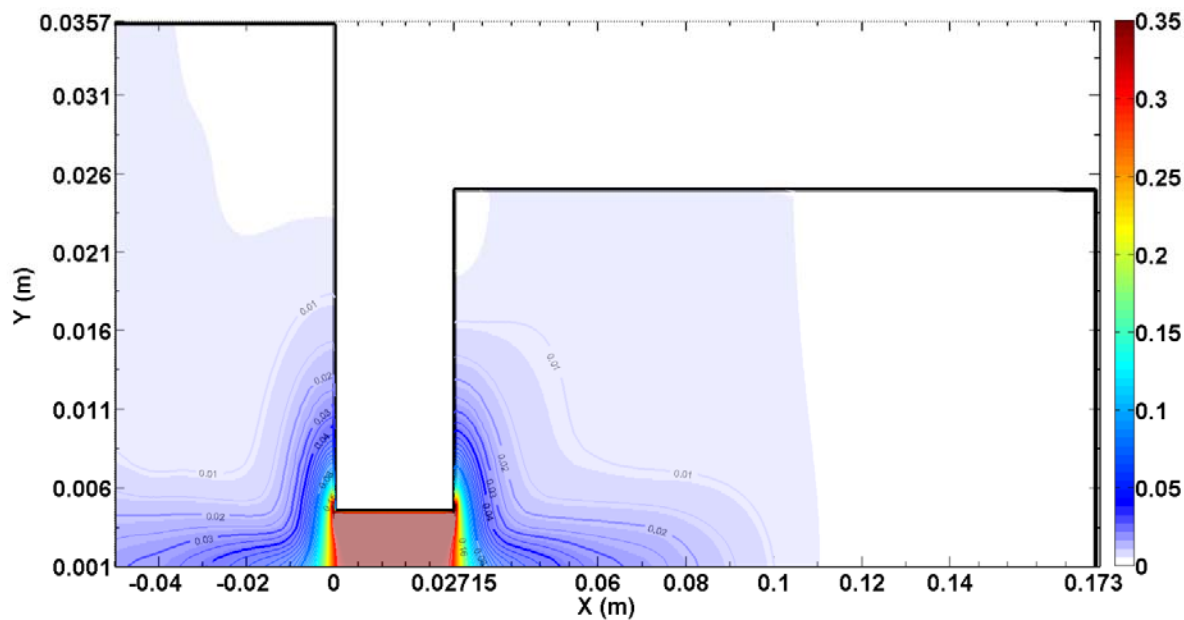
(b)

Fig. 3. Comparison of time-averaged velocity magnitude for 9mm neck diameter; (a) Volume Case 01 (b) Volume Case 14

23

Table. 2: Perforated panel structure parameters

Plate	Hole diameter (mm)	Thickness (mm)	Perforated ratio	Cavity Depth(mm)
#1	1	2	0.38%	55
#2	1	2	1.23%	55
#3	3	2	3.41%	55
#4	0.6	1	0.9%	15
#5	1	1	1%	30
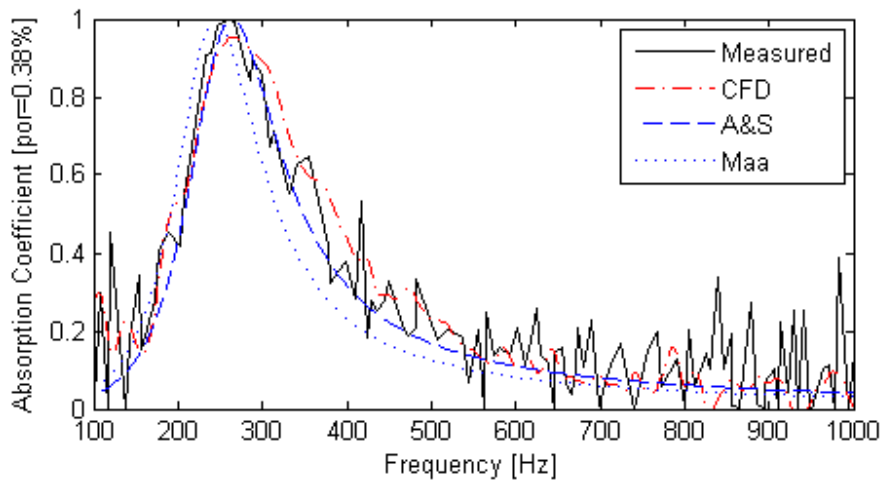
(a)
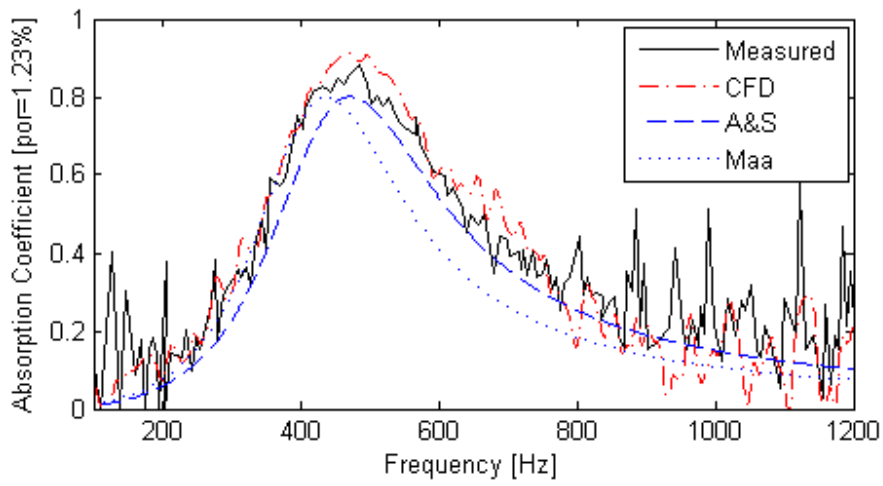
(b)
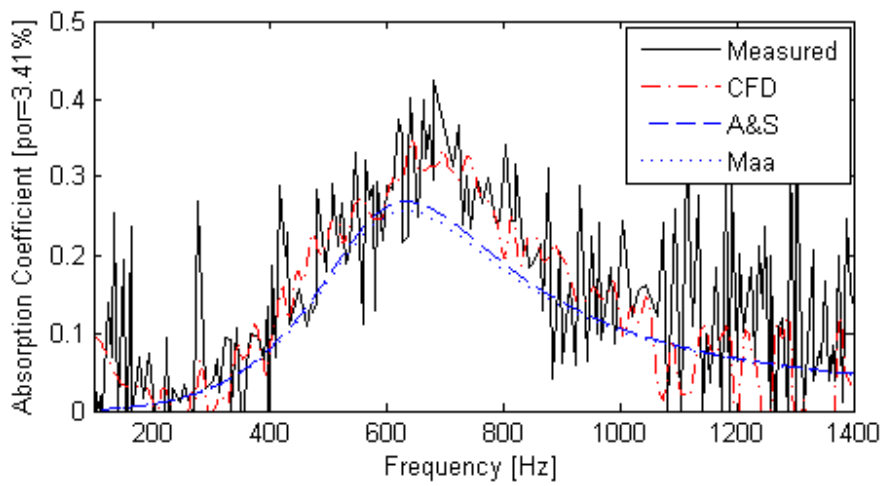
(c)

Figure.4 Absorption coefficient results comparison; (a) porosity=0.38% (b) porosity=1.23% (c) porosity=3.41%

25

Table.3 Absorption band -width comparison

Plate	Hole diameter	Porosity	Absorption coefficient	Experiment	CFD	Atalla&Sgard	Maa
#1	1mm	0.38%	>0.5	220-370Hz	210-385Hz	220-360Hz	200-340Hz
#2	1mm	1.23%	>0.5	360-650Hz	360-680Hz	375-630Hz	360-580Hz
#3	3mm	3.41%	>0.2	460-850Hz	430-850Hz	520-780Hz	530-770Hz
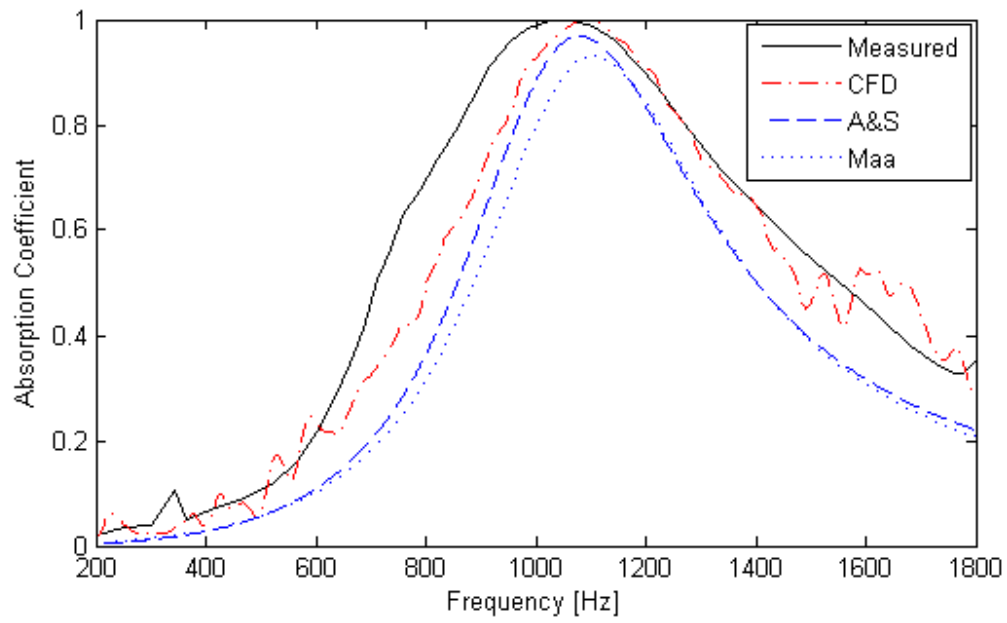
(a)
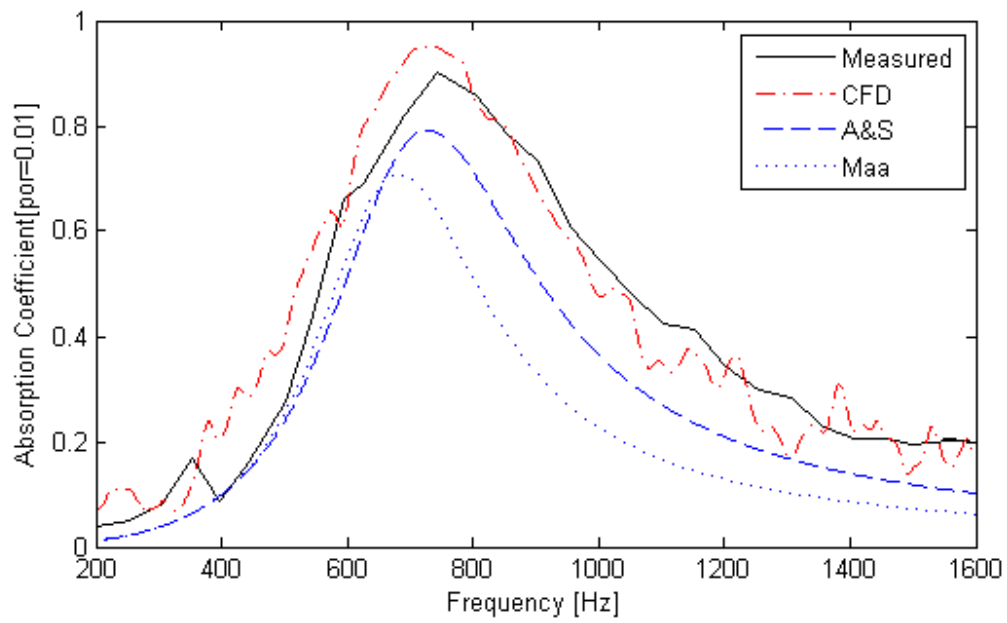
(b)

Figure.5 Absorption coefficient results comparison for the samples (a)Spec#1 in Ref. 36, (b) Ref.37

28

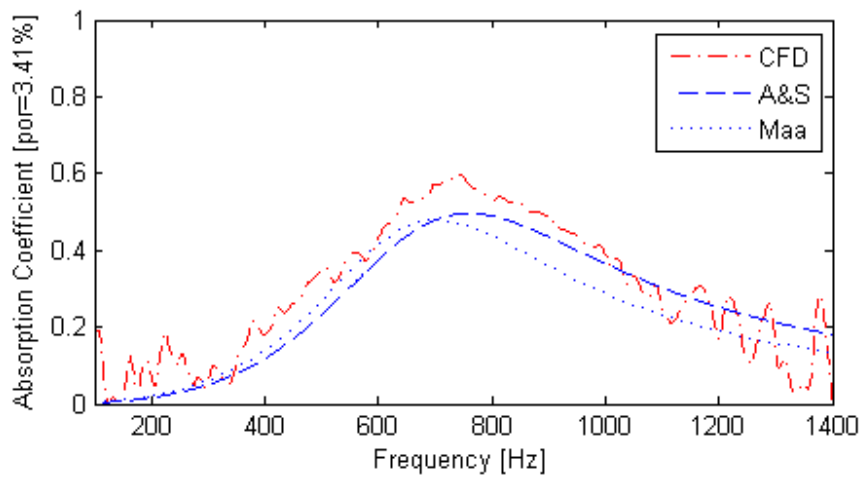Table.4 Perforated panel structure parameters and viscous resistivity

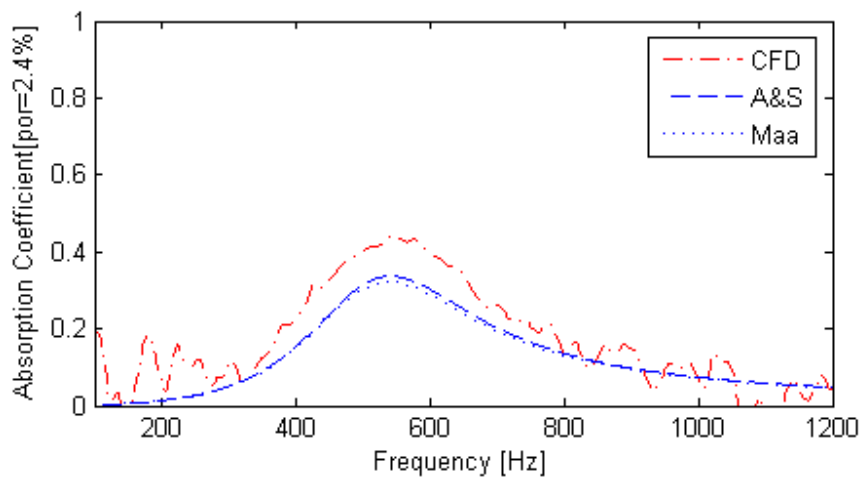| Plate	Hole diameter (mm)	Thickness (mm)	Perforated ratio
#6	1	2	0.72%
#7	1	2	2.4%
#8	1	2	3.41%
#9	3	2	1.23%
#10	3	2	2.4%
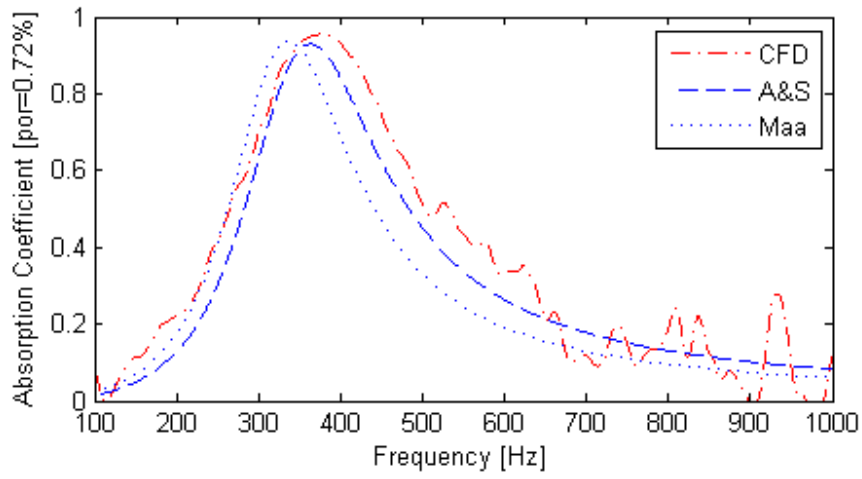
(a)
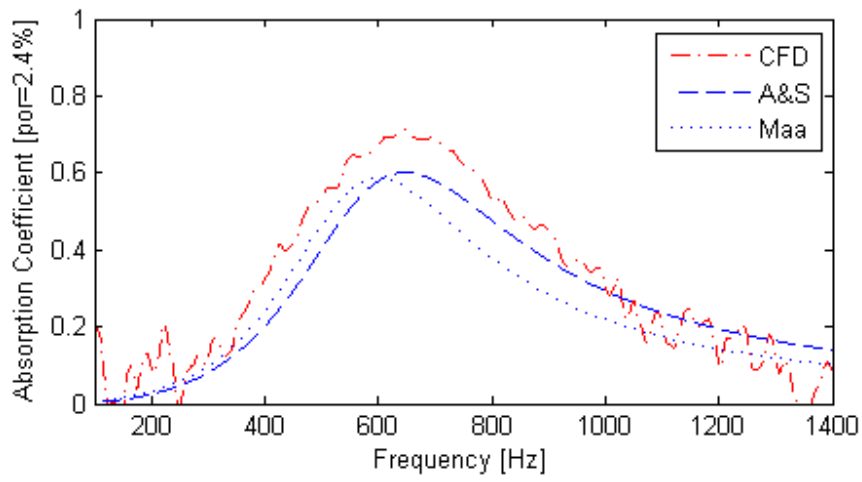
(b)

(c)

Figure.6 Absorption coefficients comparison for plate#6(a), plate#7(b) and plate#8(c)

30
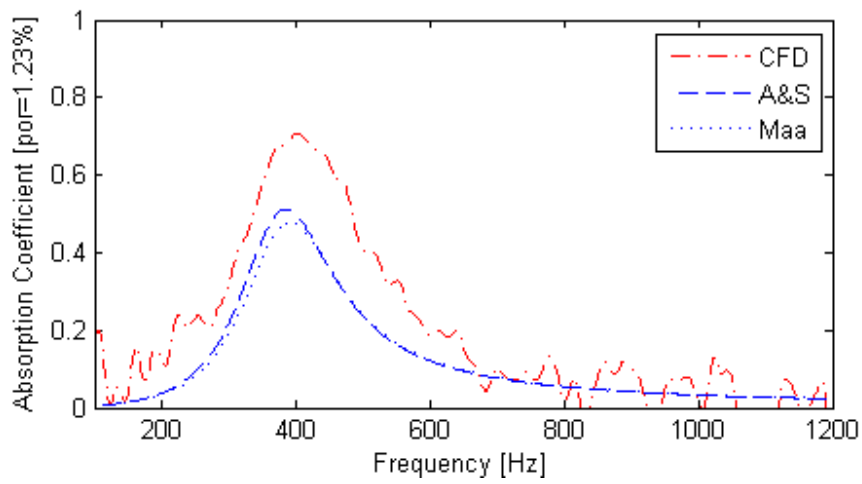
(a)

(b)

Figure.7 Absorption coefficients comparison for plate#9(a) and plate#10(b)
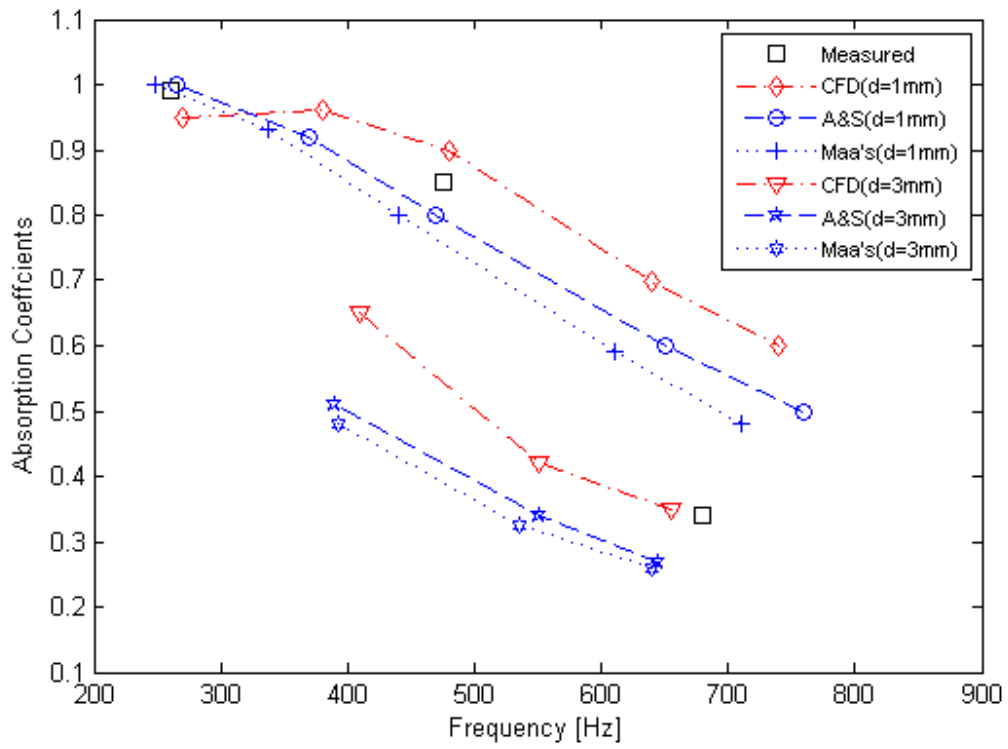
31

Figure.8 Experimental, CFD and analytical results of absorption coeffcients at resonant frequency